PERGAMON

International Journal of Heat and Mass Transfer 41 (1998) 3321–3337

International Journal of HEAT and MASS TRANSFER

The thermal–hydraulic characteristics of staggered circular finned-tube heat exchangers under dry and dehumidifying conditions

Jiin-Yuh Jang*, Jen-Tien Lai, Long-Chi Liu

Department of Mechanical Engineering, National Cheng-Kung University, Tainan, Taiwan 70101

Received 5 July 1997

Abstract

Fluid flow and heat transfer over four row circular finned-tube heat exchangers with staggered arrangement are studied experimentally and numerically. Two types of finned-tube configurations have been investigated under the dry and wet conditions for different values of inlet frontal velocity ranging from 1 to 6 m s^{-1}. The experimental results indicated that the sensible Colburn factor, J_s, and for the friction factor, f, the wet coils are, respectively 20% and 15% higher than that for the dry coils. The three-dimensional numerical results of laminar model for the dry coils are also presented. Conjugate convective heat transfer in the flow field and heat conduction in the circular fins are considered also. The numerical results for the streamline, isotherm, Nusselt number and fin efficiency are shown and compared with the experiments.

Nomenclature

A_c frontal area [m^2]
A total heat transfer area [m^2]
c_p specific heat of the fluid [kJ kg^{-1} $°C^{-1}$]
f friction factor
G mass velocity [kg $m^{-2}\cdot s^{-1}$]
h local heat transfer coefficient [W m^{-2} $°C^{-1}$]
$\bar{h}$ average heat transfer coefficient [W m^{-2} $°C^{-1}$]
h_d mass transfer coefficient [kg m^{-2}]
h_s sensible transfer coefficient [W m^{-2} $°C^{-1}$]
j Colburn factor for dry coil, $j = \frac{h}{G\cdot c_p} Pr^{2/3}$
j_s sensible Colburn factor for wet coil, $j_s = \frac{h_s}{G\cdot c_p} Pr^{2/3}$
j_t mass transfer Colburn factor for wet coil, $j_t = \frac{h_d}{G} Sc^{2/3}$
k thermal conductivity [W m^{-1} $°C^{-1}$]
KR thermal conductivity ratio of fin to the fluid [k_s/k_f]
Nu local Nusselt number, $Nu = h\cdot H/k$
$\overline{Nu}(\theta)$ average Nusselt number on the fin surface along the radial direction
Pr Prandtl number
H fin spacing [mm]
ΔP pressure drop [Pa]
q'' heat flux [W m^{-2}]
Re_H Reynolds number based on fin spacing, $Re_H = w_{in}H/v$
Sc Schmidt number
T temperature [°C]
T_{in} inlet temperature [°C]
U_i, U_j dimensionless velocity vectors
w_{in} frontal velocity [m s^{-1}].

Greek symbols
ρ density [kg m^{-3}]
η_f fin efficiency
v kinematic viscosity [m^2 s^{-1}]
σ $\sigma = A_c/A$
Θ dimensionless temperature, $\Theta = (T-T_{in})/(T_w-T_{in})$.

Subscripts
f fluid region
i inlet
m average
o outlet

* Corresponding author.

0017–9310/98 $19.00
PII: S0017-9310(98)00037-4

s solid fin region
w wall.

1. Introduction

The reported thermal–hydraulic performance data of the circular finned-tube heat exchangers were experimental in nature. A substantial amount of performance data on the dry coils has been published. Webb [1] provides a survey of the published data and correlations. He recommended the Briggs and Young [2] correlation for heat transfer, and the Robinson and Briggs [3] correlation for pressure drop. Both correlations are valid for four or more tube rows. Recently, Idem et al. [4–5] reported the convective heat and mass transfer coefficients and friction factor for a circular finned-tube heat exchanger with in-lined arrangement under the dry and wet operation conditions.

There have been a number of numerical studies on the thermal–hydraulic characteristics for three-dimensional plate-fin tube heat exchangers under the dry conditions. Yamashita et al. [6–7] used a fundamental model, consisting of a pair of parallel plates with a square cylinder perpendicular to flow through the plates, to simulate plate-fins and a tube. Three-dimensional numerical computation was performed by Matsubara et al. [8] for the developing region of flow and thermal fields in an internally rectangular finned channel. Bastani et al. [9] employed one circular tube as the computation domain and assumed that the flow was fully developed with periodic boundary condition to simulate the heat and flow field of in-lined plate-fin tube arrays. The numerical and experimental studies of three-dimensional laminar flow and heat transfer in multi-row (1–6) plate-fin and wavy-fin tube heat exchangers are examined by Jang et al. [10] and Jang and Chen [11], respectively, with whole computational domain (1–6 rows) from the fluid inlet to outlet solved directly. All of the works mentioned above are based on the assumption that the fin temperatures are isothermal, which would be true only when the fin conductivity is very large. As the fin conductivity is finite, heat transfer in finned-tube heat exchanger is a conjugate problem, requiring computation of three-dimensional flow and temperature field and heat conduction in the fin. Conjugate heat transfer for a plate-fin tube heat exchanger was recently investigated by Fiebig et al. [12]. It could be noted that the corresponding problem for a circular-fin tube heat exchanger, to the author's knowledge, does not seem to have been investigated.

No related experimental work on the circular finned-tube heat exchangers with staggered arrangement under the wet condition has been published. This has motivated the present investigation. Experiments were conducted in a steady-state induced draft wind tunnel. In addition, numerical simulations of the laminar, three-dimensional fluid flow and heat transfer over the 4-row dry circular finned-tube banks are performed. Conjugate convective heat transfer in the flow field and heat conduction in the circular fins are considered also. The numerical results for the streamline, isotherm, Nusselt number and fin efficiency are compared with the experiments.

2. Experimental set-up and data reduction

Two types of finned-tube configurations were tested and their detailed geometrical parameters are tabulated in Table 1. Experiments were conducted in an induced open wind tunnel as shown in Fig. 1. The ambient temperature and humidity were controlled at 27°C and 70% by an air-ventilator which can provide a cooling capacity up to 21.2 kW. The air flow was driven by a 3.73 kW centrifugal fan with an inverter to provide various inlet velocities. The air temperatures at the inlet and exit zones across the test section were measured by two psychometric boxes which are constructed based on ASHRAE 41.1 standard [13]. The pressure of the test coil is detected by a precision differential pressure transducer, readings to 0.1 Pa. The air flow measuring station is an outlet chamber setup with multiple nozzle based on the ASHRAE 41.2 [14].

The working medium in the tube side was hot or chilled water. The water temperature was controlled by a thermostat reservoir. In dry conditions, the hot water inlet temperature was controlled at 75°C; in wet condition, the chilled water was controlled at 7°C. Both the water side inlet and outlet temperatures were measured by two precalibrated RTDs (pt-100Ω). Their accuracy was within 0.05°C. The water volumetric flow rate was measured by a magnetic volume flow meter with 0.002 l s^{-1} resolution. All the data signals were collected and converted by a data acquisition system (a hybrid recorder). The data acquisition system then transmitted the converted signals through GPIB interface to the host computer for further operation. Generally, the energy balance between air side and tube side was 3% for dry coils and 7% for wet coils. To obtain the average heat transfer coefficients h for the dry coils and the sensible heat transfer coefficient h_s and mass transfer coefficient h_d for the wet coils from the measured experimental data, the ε-NTU (effectiveness-number of transfer unit) method was used for the dry coils and LMHD (log mean enthalpy difference) method was applied for the wet coils. The water side resistance was estimated to be less than 10% of the overall heat resistance. Noting that the wall resistance was negligible, the dominant thermal resistance was always on the air side. This may resolve any concern about the magnitude and accuracy of the water side that is being subtracted from the overall resistance.

The heat and mass transfer characteristics of the heat

Table 1
Heat exchangers geometrical data

	Sample A	Sample B
Inside diameter D_i (mm)	14.8	23.2
Outside diameter D_o (mm)	19.1	27
Fin outer diameter D_e (mm)	43	41
Fin height s (mm)	12	7
Fin thickness δ (mm)	0.4	0.5
Fin spacing H (mm)	3.4	3.5
Transverse pitch X_T (mm)	63	42
Longitudinal pitch X_L (mm)	54.6	37
Hydraulic diameter D_h (mm)	11.4	6.5
Tube numbers	24	24
Pass numbers	4	4
HX length (mm)	400	400
HX width (mm)	266	148
HX height (mm)	350	280
Tube material	Carbon steel	Carbon steel
Fin material	Carbon steel	Carbon steel

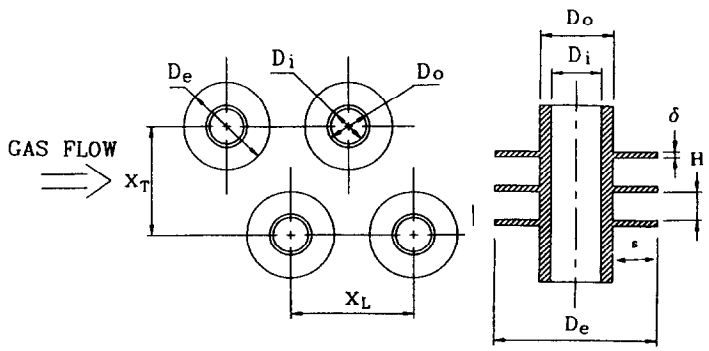

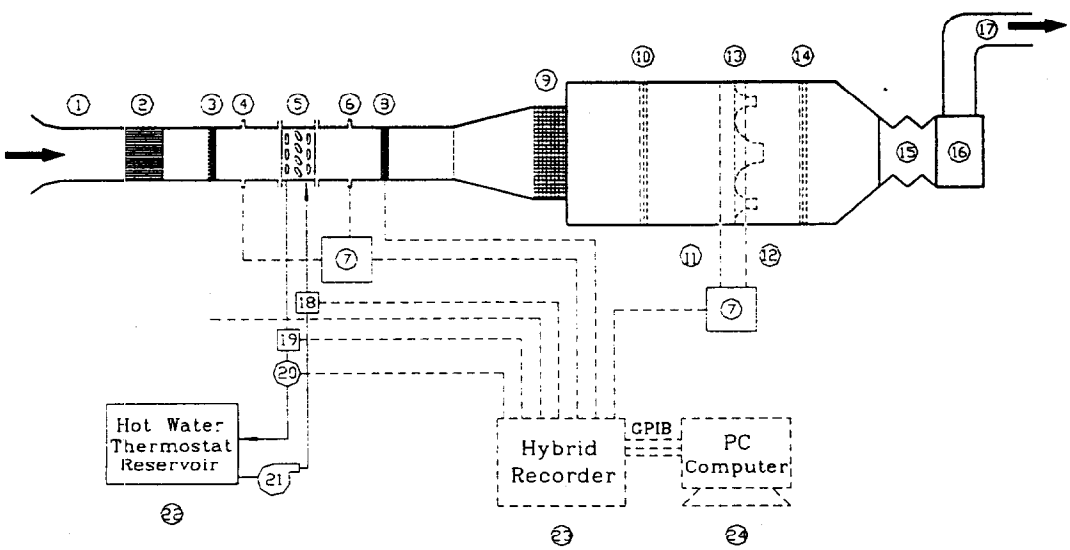

Fig. 1. Schematic diagram of the experimental set-up.

exchangers are presented in the following non-dimensional groups:

Colburn factor j for dry coil

$$j = \frac{h}{G \cdot c_p} Pr^{2/3} \tag{1}$$

sensible Colburn factor J_s for wet coil

$$j_s = \frac{h_s}{G \cdot c_p} Pr^{2/3} \tag{2}$$

mass transfer Colburn factor J_t for wet coil

$$j_t = \frac{h_d}{G} Sc^{2/3} \tag{3}$$

Here, G is the mass velocity, c_p is the specific heat of the fluid, Pr and Sc are the Prandtl and Schmidt numbers, respectively. All the fluid properties are evaluated at the average values of the inlet and outlet temperatures.

The core friction factor f of the heat exchanger is calculated from the pressure drop equation proposed by Kay and London [15], including the entrance and exit pressure loss coefficient K_c and K_e.

$$f = \frac{A_c \rho_m}{A \rho_i}\left[\frac{2\rho_i \Delta P_o}{G_o^2} - 2\left(\frac{\rho_i}{\rho_o} - 1\right) - (K_i + 1 - \sigma) + \frac{\rho_i}{\rho_o}(1 - \sigma - K_e)\right] \tag{4}$$

Uncertainties in the reported experimental values of J, J_s, mass transfer Colburn factor J_t and friction factor f, as estimated by the method suggested by Moffat [16], range from 4% to 7%.

3. Three-dimensional mathematical analysis

3.1. Governing equations

The fluid is considered incompressible with constant properties and the flow is assumed to be laminar, steady, and no viscous dissipation. The dimensionless equations for continuity, momentum and energy in the fluid air region may be expressed in tensor form as:

$$\frac{\partial U_i}{\partial X_i} = 0 \tag{5}$$

$$\frac{\partial}{\partial X_j}(U_i U_j) = -\frac{\partial P}{\partial X_i} + \frac{1}{Re_H}[\nabla^2 U_i] \tag{6}$$

$$\frac{\partial}{\partial X_j}(\Theta_f U_j) = \frac{1}{Re_H Pr}[\nabla^2 \Theta_f] \tag{7}$$

The energy heat conduction equation for the solid fin region will be

$$\nabla^2 \Theta_s = 0 \tag{8}$$

Here, the velocity has been nondimensionalized with the uniform inlet velocity w_{in} at the channel inlet; all the length coordinates with the fin spacing H; the pressure normalized with ρw_{in}^2; the dimensionless temperature is defined as $\Theta = (T - T_{in})/(T_w - T_{in})$ and the Reynolds number is $Re_H = w_{in} \cdot H/v$.

3.2. Boundary conditions

Because the governing equations are elliptic in spatial coordinates, the boundary conditions are required for all boundaries of the computation domain. At the upstream boundary, uniform flow with the velocity $w_{in}\vec{k}$ and temperature T_{in} (=300 K) are assumed. At the downstream end of the computational domain, located seven tube diameters from the last downstream row tube, streamwise gradient (Neumann boundary conditions) for all variables are set to zero. At the symmetry planes normal gradients are equal to zero. At the solid surfaces, no-slip conditions for the velocity are specified. In addition, at the fin surface

$$\Theta_f = \Theta_s, \frac{\partial \Theta_f}{\partial X} = KR \frac{\partial \Theta_s}{\partial X} \tag{9}$$

Equation (9) represents the condition of continuity of temperature and heat flux on the fin surface, where $KR = k_s/k_f$ is the thermal conductivity ratio of the fin to the fluid. At tube surface, constant wall temperature T_w (=350 K) are assumed.

$$\Theta_f = \Theta_w = 1. \tag{10}$$

3.3. Nusselt number and fin efficiency

The local heat transfer coefficient h is defined as

$$h = \frac{q''}{T_w - T_b} \tag{11}$$

where q'' is the local heat flux and T_b is the local bulk mean temperature of the fluid. The local heat transfer coefficient can be expressed in the dimensionless form by the Nusselt number Nu, defined as:

$$Nu = \frac{h \cdot H}{k} = \frac{\partial\left[\frac{\Theta}{\Theta_b}\right]_{wall}}{\partial n} \tag{12}$$

where $\Theta_b = (T_b - T_{in})/(T_w - T_{in})$ is the local dimensionless bulk mean temperature and n is the dimensionless unit vector normal to the wall.

The fin efficiency η_f is defined as

$$\eta_f = \frac{(Q_{fin})_{actual}}{(Q_{fin})_{maximum}} = \frac{[\int\int q''(y,z)\,dy\,dz]_{fin=T_s}}{[\int\int q''(y,z)\,dy\,dz]_{fin=T_w=constant}} \tag{13}$$

4. Numerical method

The body-fitted coordinate along with multi-block system was used to generate a general curvilinear coordinate system numerically by solving Laplace equations with

proper control of grid densities. The governing equations are solved numerically using a control volume based finite difference formulation. The SIMPLEC algorithm [17] is used to solve iteratively the system of finite-difference equations. The hybrid scheme is employed for the treatment of convection and diffusion terms. A grid system of $15 \times 19 \times 200$ grid points for sample A is adopted in the computation domain as shown in Fig. 2, while $9 \times 11 \times 152$ grid points are used for sample B. However, a careful check for grid-independence of numerical solutions has been made for the accuracy and validity of the numerical results. For this purpose, three different grid systems, $16 \times 21 \times 219$, $15 \times 19 \times 200$, $13 \times 17 \times 179$ for sample A $11 \times 13 \times 196$, $9 \times 11 \times 152$, $7 \times 9 \times 108$ for sample B, are tested. It is found that for $w_{in} = 2$ m s^{-1}, the relative errors in the local pressure and temperature are less than 1%. Computations were performed on IBM/RS6000 and typical CPU times are 4–11 h for each case.

5. Results and discussions

Experimental results of thermal–hydraulic characteristics for the samples A and B under the dry and wet operations are illustrated in Figs. 3–6. Figures 3 and 4 present the variation of the Colburn j factor and sensible Colburn J_s factor with the Reynolds number Re for the dry and wet coils, respectively. Also plotted in the figures for the comparison are the correlations developed by Briggs and Young [2] for the dry staggered coils and Idem et al. [4] for the wet coils, which is under the in-lined arrangement. The present dry coil results are in good agreement with those of the Briggs and Young [2], while for the wet coils, the correlation developed by Idem et al. [4] is 30–50% lower than that of the present experimental results. By comparing Figs. 3 and 4, it can be seen that the sensible Colburn factor J_s for the wet coils is 20% higher than the j factor for the dry coils. The variation of the mass transfer Colburn j_t factor with the Reynolds number is illustrated in Fig. 5. Again, the j_t value for the in-lined arrangement [4] is 50–100% smaller than that for the staggered arrangement. Figure 6 shows the dry and wet friction factor f vs Re for samples A and B. It is noted that the dry friction correlation obtained by Robinson and Briggs [3] is also illustrated in the figure. It is seen that friction factor f for the wet coils is 15% higher than that for the dry coils. The correlation of Idem et al. [4] for the in-lined arrangement is significantly lower

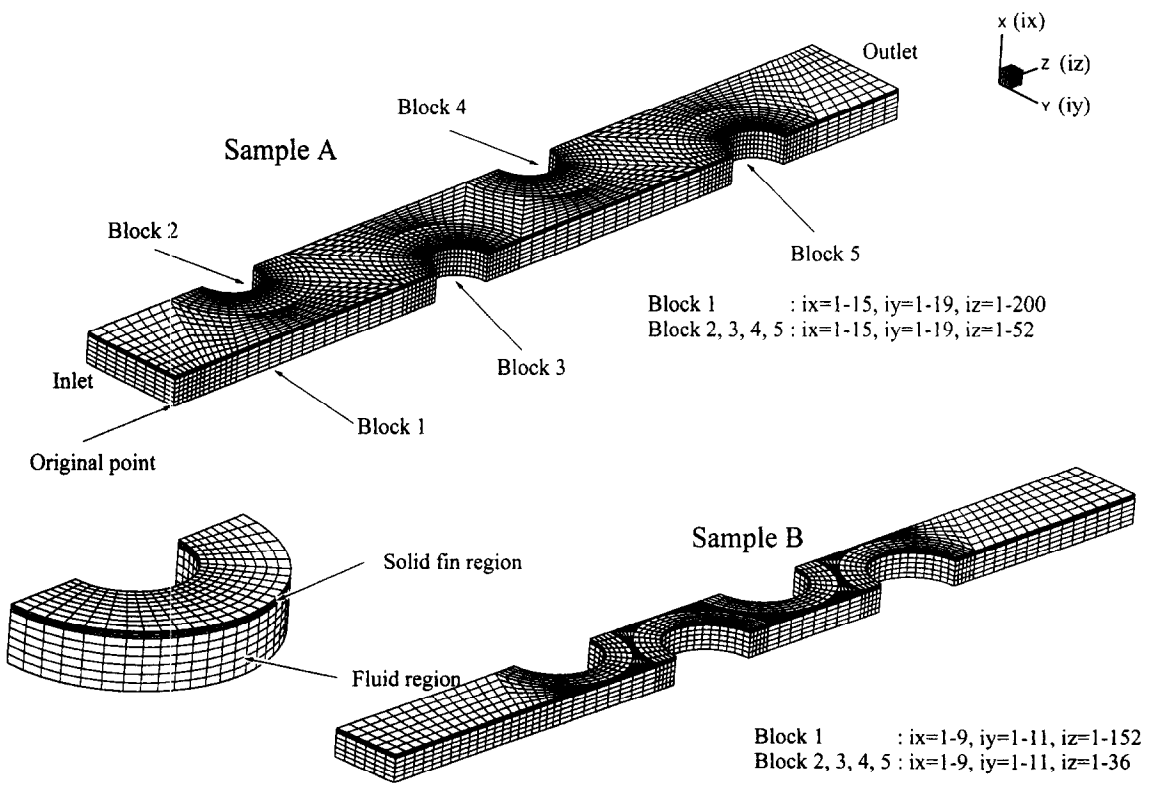

Fig. 2. Computational grid system for samples A and B.

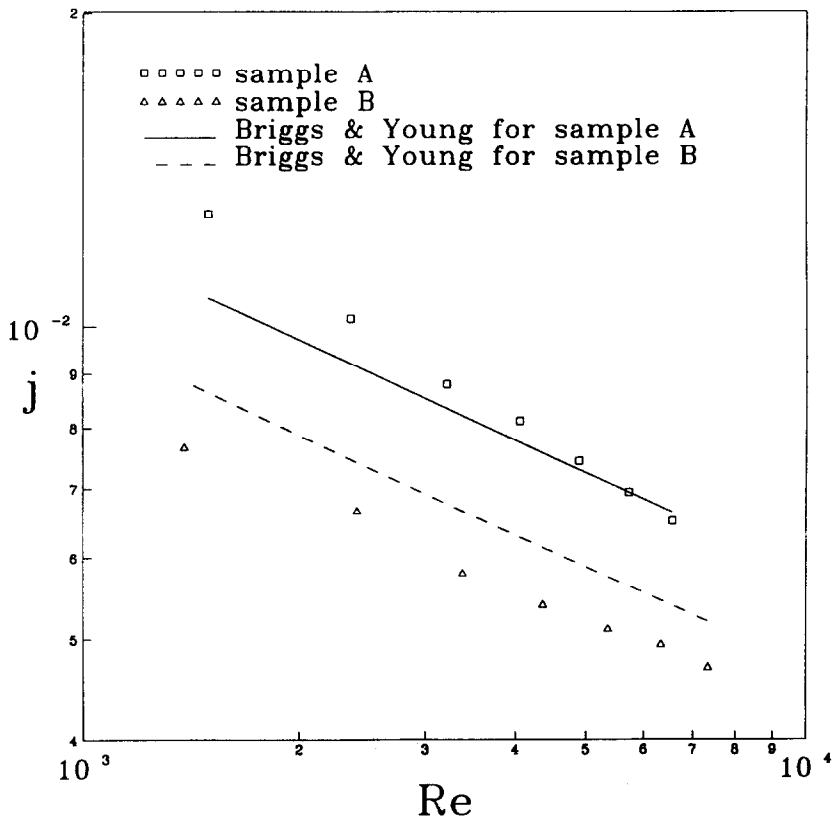

Fig. 3. The variations of j factors with Re for the dry coils.

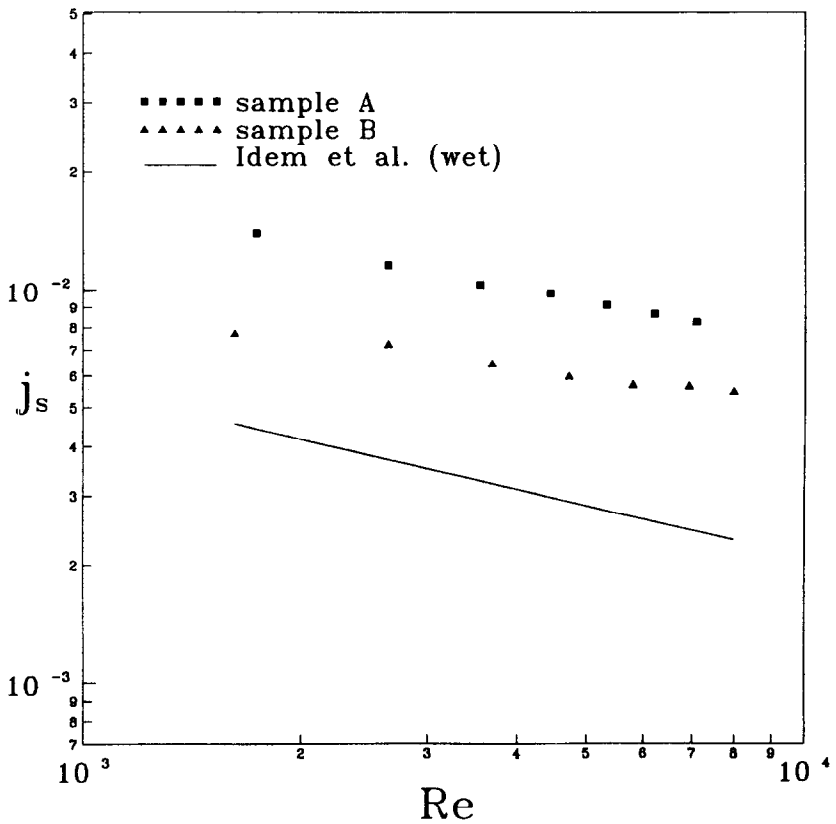

Fig. 4. The variations of j_s factor with Re for the wet coils.

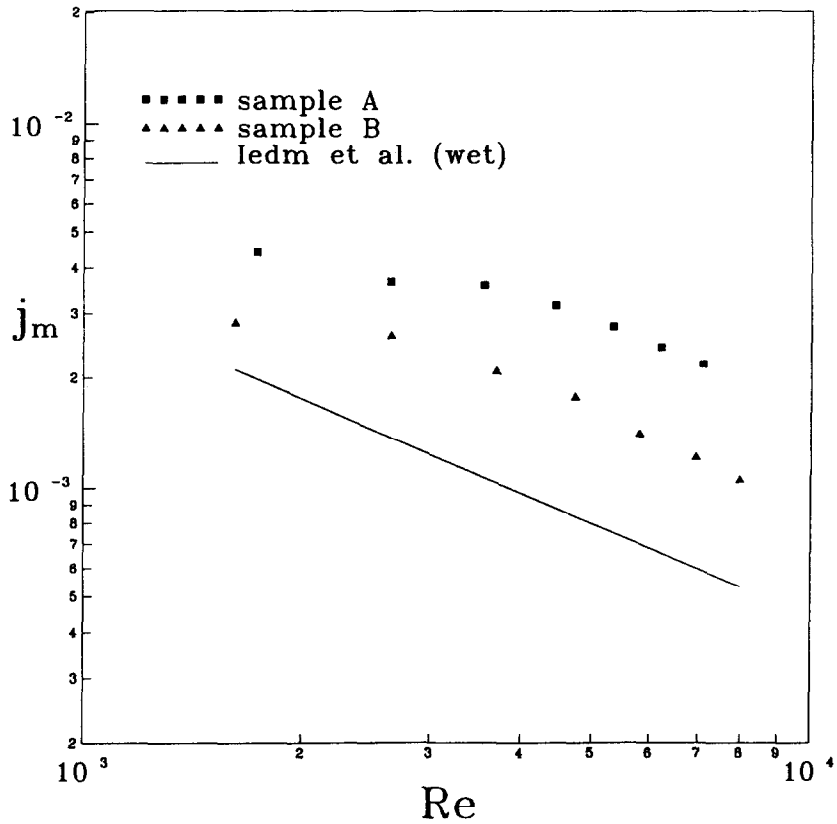

Fig. 5. The variations of j_t factor with Re for the wet coils.

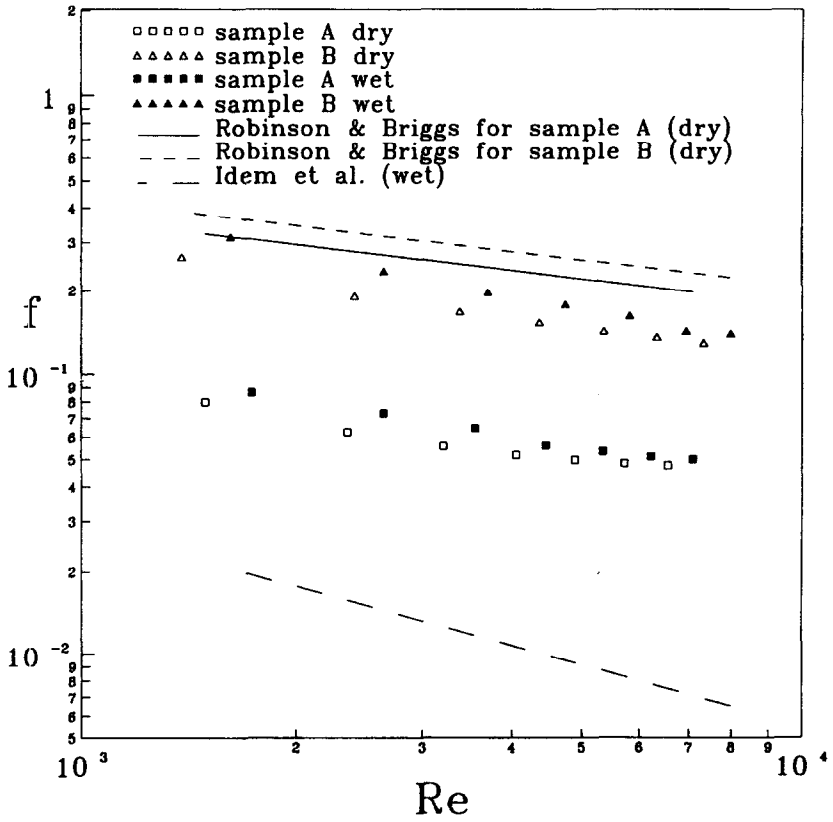

Fig. 6. The dry and wet friction factors f vs Re.

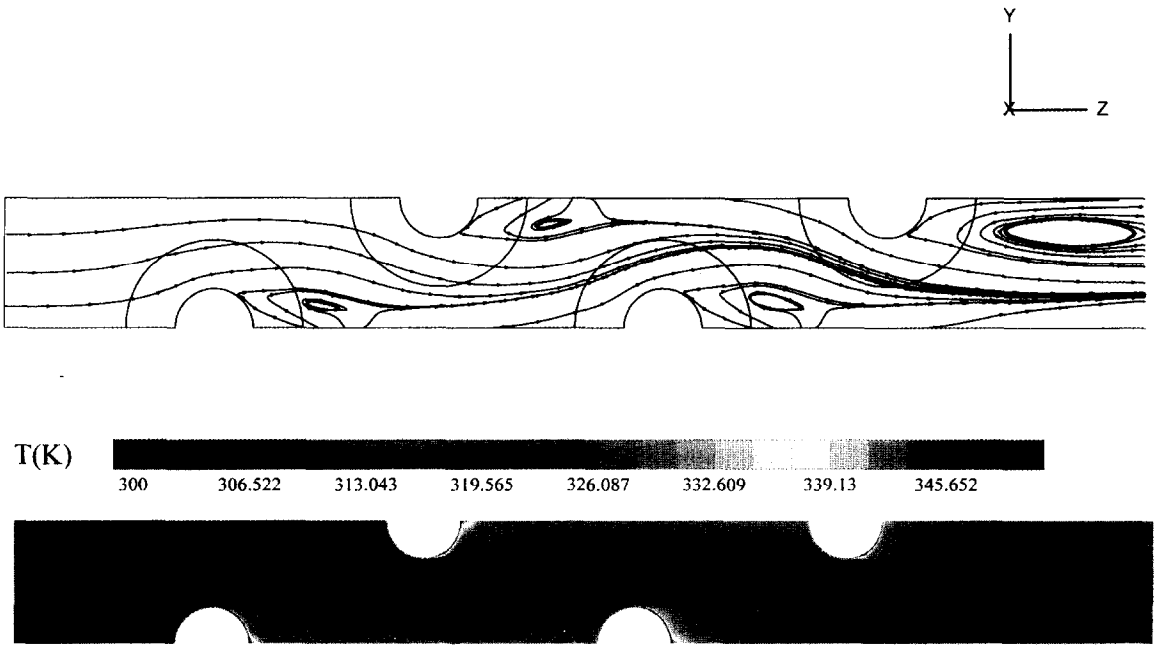

(a) X = 0

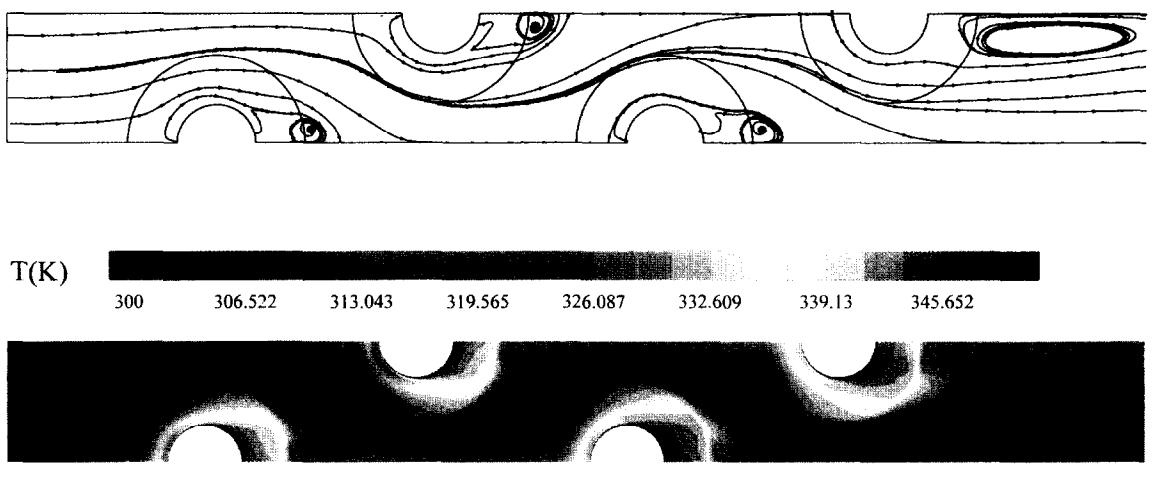

(b) X = 0.4

Fig. 7. The streamline and isotherm patterns for sample A on the yz-plane for $w_{in} = 3\ m\ s^{-1}$ at $X = 0$ (near the mid-plane) and $X = 0.4$ (near fin surface).

(a) X = 0

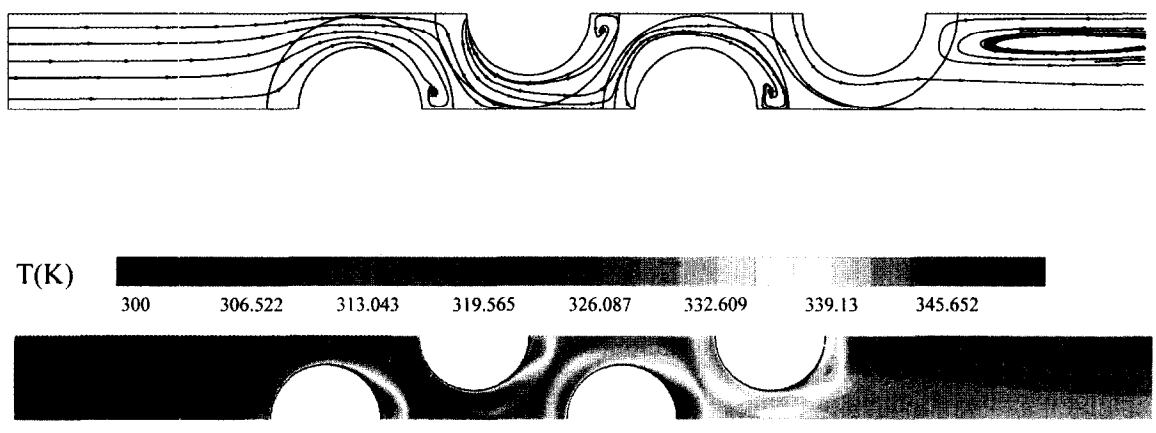

(b) X = 0.4

Fig. 8. The streamline and isotherm patterns for sample B on the yz-plane for $w_{in} = 3\ m\ s^{-1}$ at $X = 0$ (near the mid-plane) and $X = 0.4$ (near fin surface).

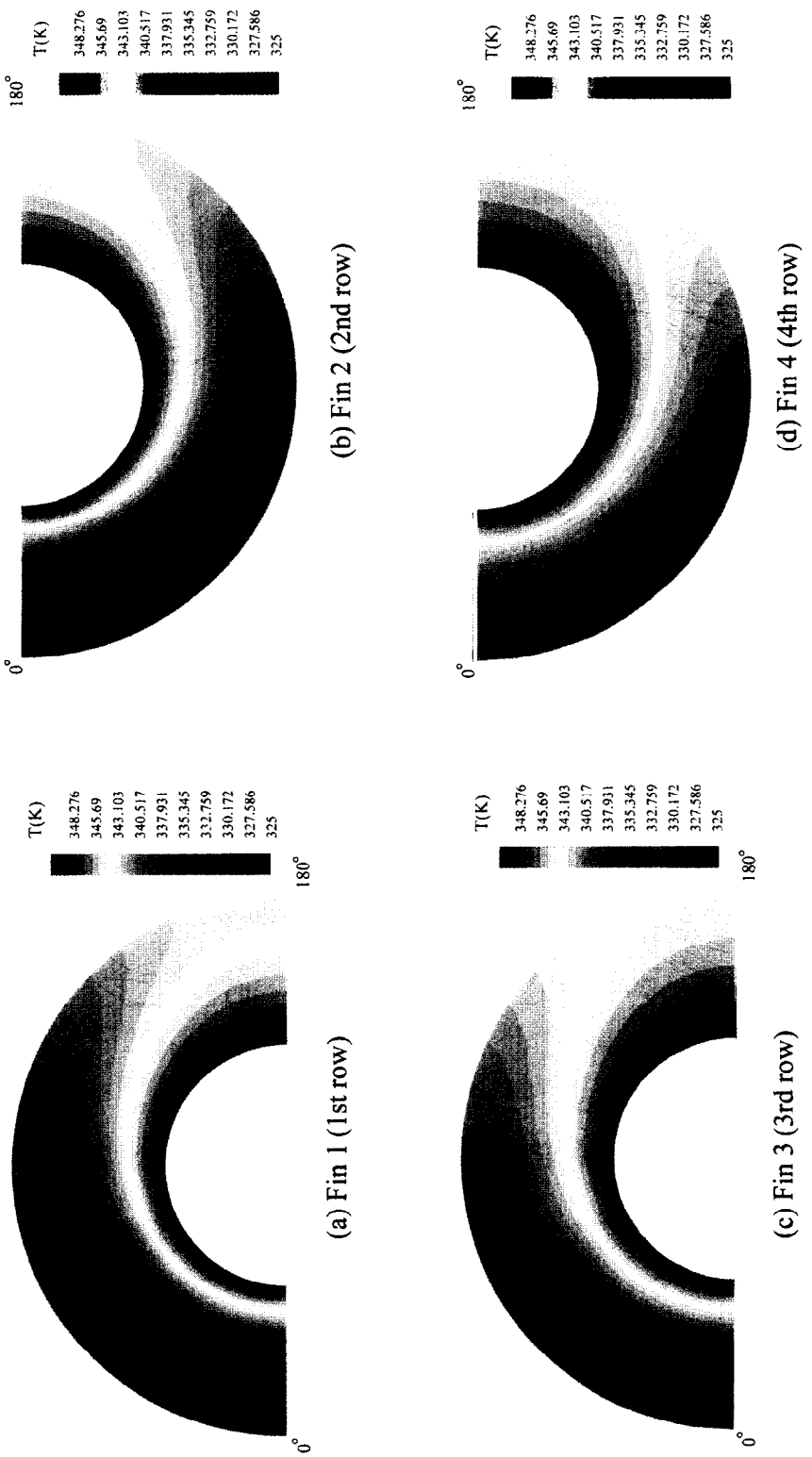

Fig. 9. The fin surface temperature contours for sample A.

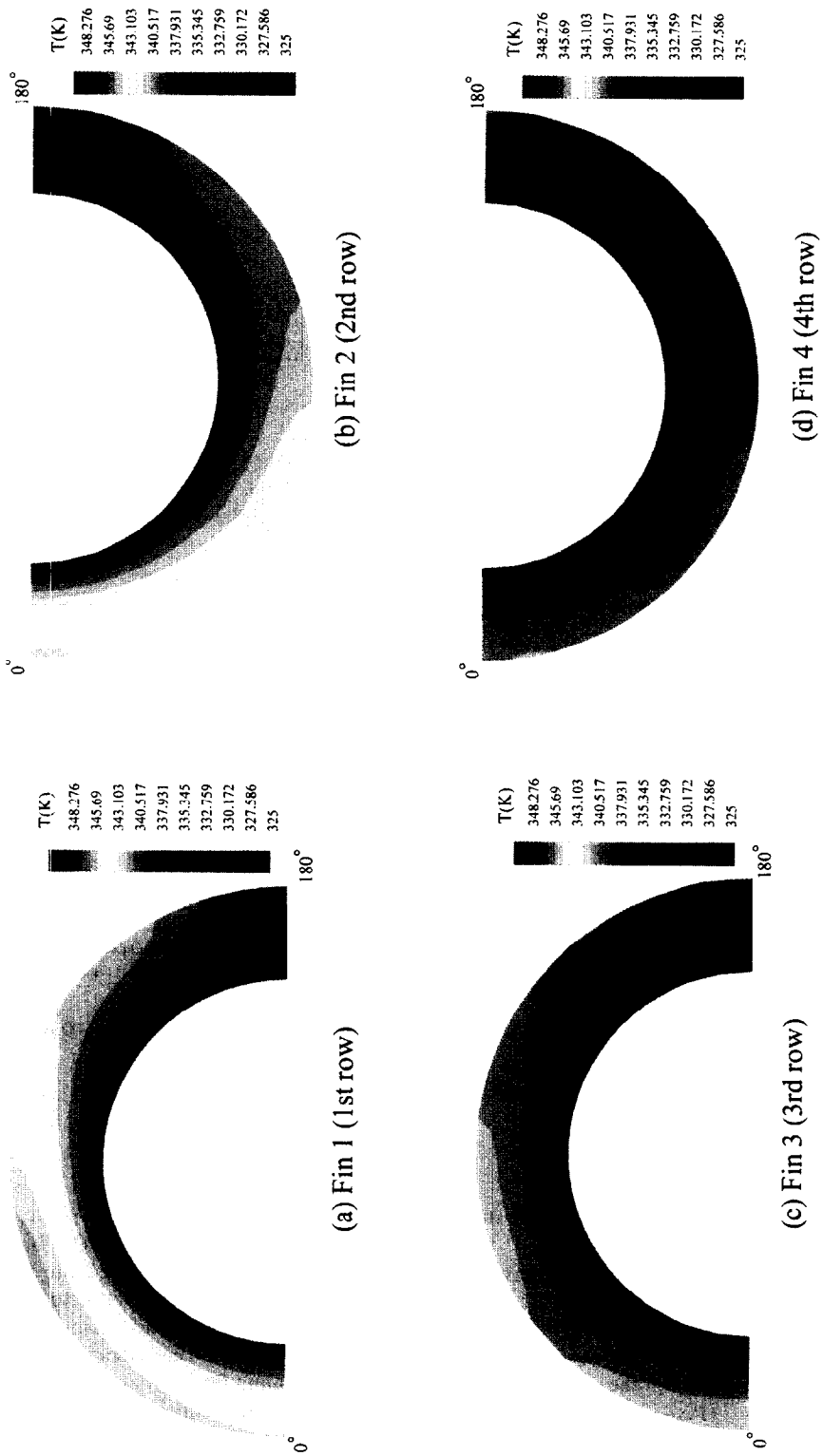

Fig. 10. The fin surface temperature contours for sample B.

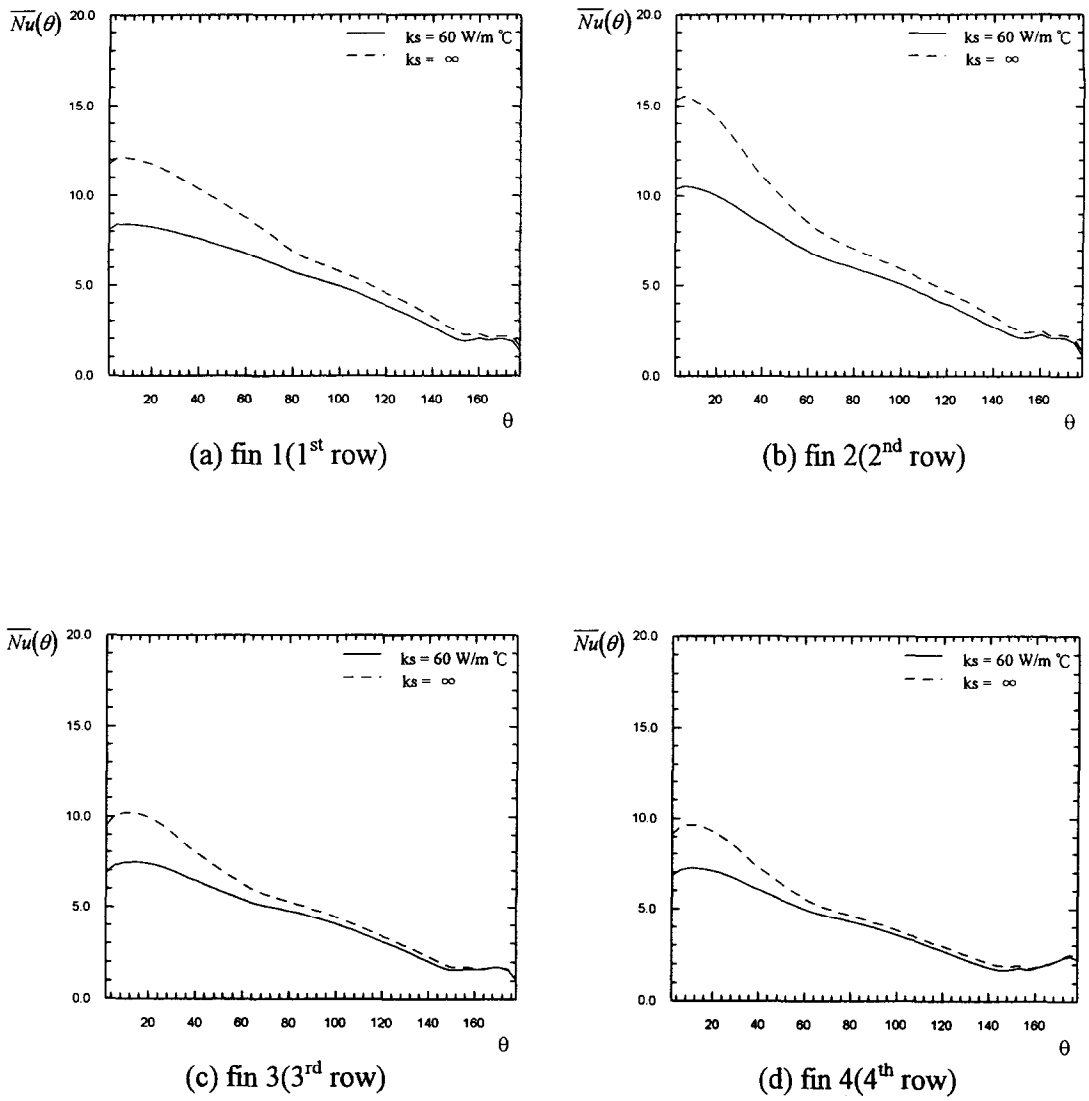

Fig. 11. $\overline{Nu}(\theta)$ vs θ from the 1st to the 4th row for sample A.

than that of the present experimental results for the staggered arrangement.

The numerical simulations of the three-dimensional laminar circular finned-tube bank under the dry condition are shown in Figs. 7–12. Figures 7 and 8 illustrate the streamline and isotherm patterns for samples A and B, respectively, on the yz-plane for the case with inlet frontal velocity $w_{in} = 3\ \mathrm{m\ s^{-1}}$ ($Re_H = 671$) at $X = 0$ (near the mid-plane between two fins) and $X = 0.4$ (near the fin surface). It is seen that the flow pattern and temperature contour on the yz plane near the mid-plane ($X = 0$) and near the fin surface ($X = 0.4$) are quite different. There is a smaller backflow zone at the rear of the tube near the fin surface; while near the mid-plane, there is a larger recirculation zone behind the tube. It is also noted that the streamlines of sample B are more distorted compared to those of sample A. This is due to the fact that sample B has a larger tube outside diameter and smaller tube pitch, which results in a smaller hydraulic diameter based on the minimum free flow areas as shown in Table 1.

The fin surface temperature contours from the 1st to 4th row for samples A and B are shown in Figs. 9 and 10, respectively. The angle $\theta = 0$ corresponds to the stagnation point of each tube. The temperature distributions on the fin surfaces are significantly different from the 1st row to the 4th row; and for each fin, there is a larger

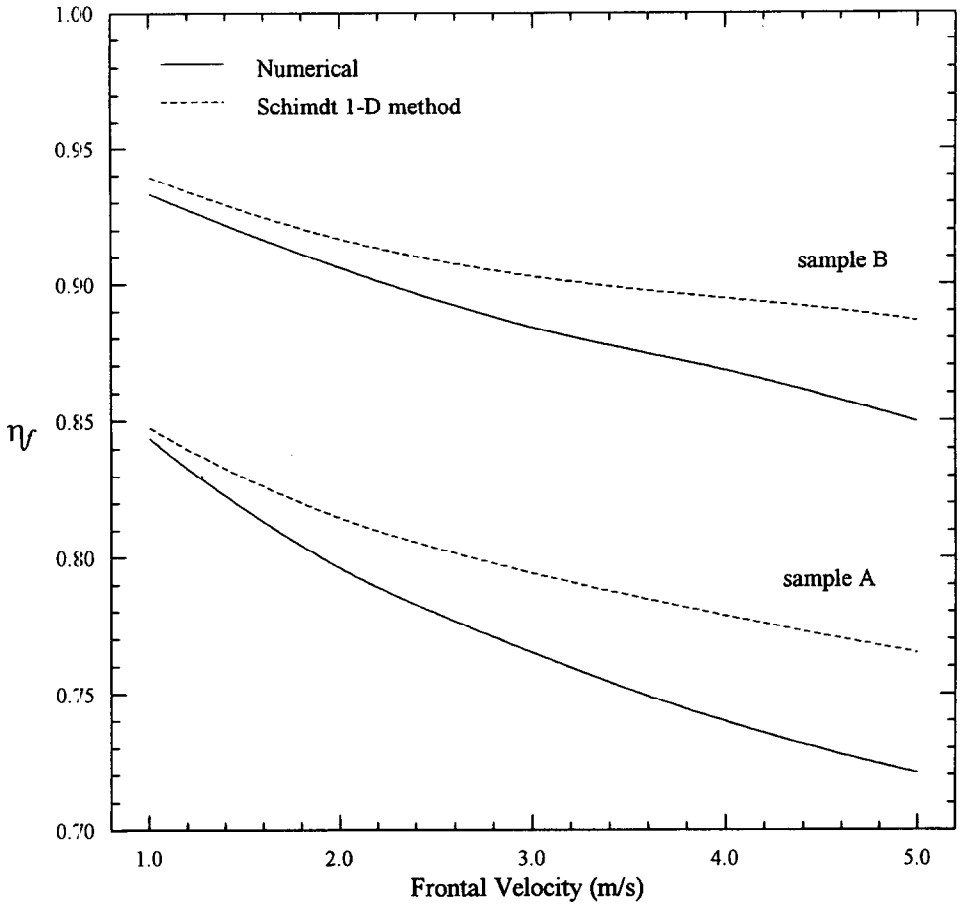

Fig. 12. Fin efficiency η_f of the 1st row vs W_{in} for sample A and B.

temperature gradient along the radial direction near the stagnation point due to the thinner thermal boundary layer. In addition, from Table 1, sample A has a larger fin height ($s = 12$ mm) than sample B ($s = 7$ mm), thus the temperature gradients along radial direction for sample A are larger compared to those of sample B as can be observed from the figures.

The variations of the average Nusselt number $\overline{Nu}(\theta)$ on the fin surface, which is integrated along the radial direction r, i.e. $\overline{Nu}(\theta) = \int Nu(r,\theta)\,dr/\int dr$, around angle θ from the 1st to the 4th row for sample A are presented in Fig. 11. As would be expected, the $\overline{Nu}(\theta)$ decreases with increasing of θ due to the growth of thermal boundary layer. As seen, the 2nd row fin has the highest peak value of $\overline{Nu}$. The dashed lines appearing in the figures represent the results for the assumption of isothermal fin (i.e. $k_s = \infty$). It is seen that the isothermal fin assumption overestimates the $\overline{Nu}(\theta)$ and the discrepancy becomes less as θ increases.

Figure 12 illustrates the variation of circular fin efficiency η_f for the 1st row as function of the various inlet front velocity ranging from 1 to 5 m s^{-1} for sample A and B. The one-dimensional closed form solutions obtained by Schmidt [18] are also shown for the comparison. As expected, the fin efficiency is decreased as the frontal velocity increases due to the increase of the average heat transfer coefficient. A close look at Fig. 12 indicates that one dimensional approximation overestimates the fin efficiency and the error is increased as the fluid velocity increases. For $w_{in} = 2$ m s^{-1}, the error is about 2%, while for $w_{in} = 5$ m s^{-1}, the error is up to 6%.

The calculated and measured pressure drop and averaged heat transfer coefficient for the dry coils at various inlet front velocity w_{in} ranging from 1 to 6 m s^{-1} are presented in Fig. 13(a) and (b), respectively. The solid lines represent the numerical results for the samples A and B; while the experimental results are denoted by the triangular and square symbols, respectively. The dashed

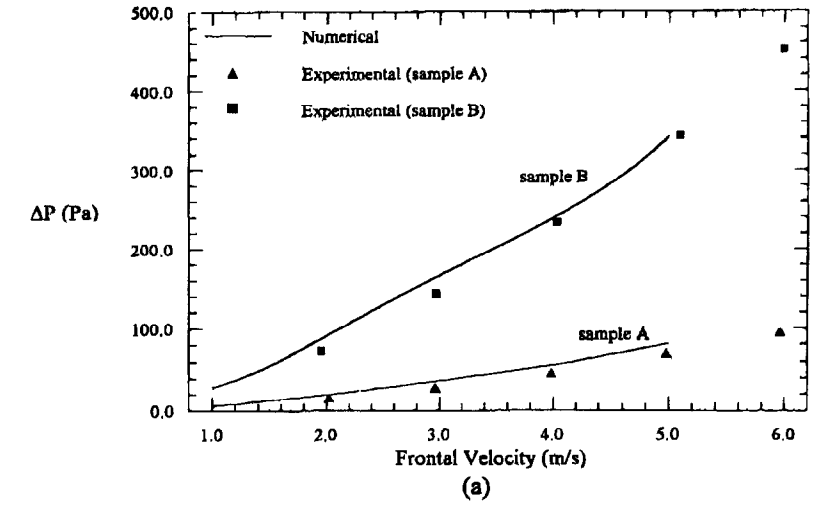

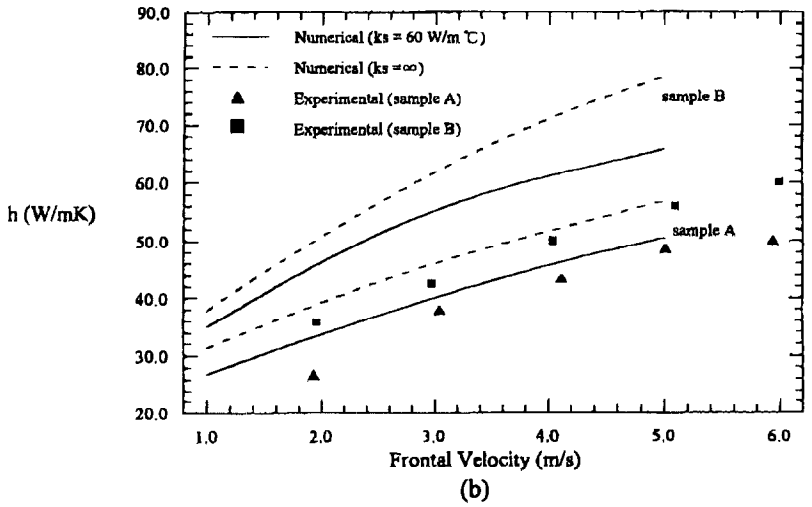

Fig. 13. The calculated and measured ΔP and $\bar{h}$ for the dry coils vs w_{in}.

lines denote the cases of isothermal fin approximation (i.e. $k_s = \infty$). It is seen that the isothermal fin approximation overpredicts the heat transfer coefficient by about 5–35%. The numerical results for the pressure drop are in excellent agreement with the experimental data. Although both the calculated and experimental results of the average heat transfer coefficients are in the same order of magnitude, the numerical results overestimate the heat transfer coefficient by 20–30%. This may be due to the fact that, the actual boundary conditions for the tube surfaces in the experiment do not occur under the constant wall temperature.

6. Conclusions

Experimental measurements of thermal–hydraulic characteristics of circular finned-tube heat exchangers under the dry and wet operation conditions are presented. The sensible Colburn factor, J_s, for the wet coils is 20% higher than that for the dry coils; the friction factor, f, for the wet coils is 15% higher than that for the dry coils. The numerical results of three-dimensional laminar flow and heat conduction in the fin for the dry coils are also performed, demonstrate that the one-dimensional approximation overestimates the fin efficiency and the

error is increased as the fluid velocity increases. It is also shown that isothermal fin approximation overpredicts the heat transfer coefficient by about 5–35%. The numerical results of dry coils for the pressure drop are in excellent agreement with the experimental data.

Acknowledgement

Financial support for this work was provided by the National Science of Taiwan under contract NSC86-2212-E006-077.

References

[1] Webb PL. Principles of Enhanced Heat Transfer, John Wiley and Sons, Inc., New York, 1994.
[2] Briggs DE, Young EH. Convection heat transfer and pressure drop of air flowing across triangular pitch banks of finned tubes. Chem Eng Prog Symp Ser 1963;59(41):1–10.
[3] Robinson KK, Briggs DE. Pressure drop of air flowing across triangular pitch banks of finned tubes. Chem Eng Prog Symp Ser 1966;62(64):177–84.
[4] Idem SA, Jacobi AM, Goldschmidt VM. Heat transfer characterization of a finned-tube heat exchanger (with and without condensation). Transaction of the ASME 1990;112:64–70.
[5] Idem SA, Goldschmidt VM. Sensible and latent heat transfer to a baffled finned-tube heat exchanger. Heat Transfer Engineering 1993;14(3):26–35.
[6] Yamashita H, Kushida G, Izumi R. Fluid flow and heat transfer in a plate-fin and tube heat exchanger (analysis of fluid flow around a square cylinder situated between parallel plates. Bulletin of JSME 1986;29(254):2562–9.
[7] Yamashita H, Kushida G, Izumi R. Fluid flow and heat transfer in a plate-fin and tube heat exchanger (analysis of fluid flow around a square cylinder situated between parallel plates). Bulletin of JSME 1986;29(258):4185–91.
[8] Matsubara K, Nakabe K, Suzuki K. A three-dimensional numerical study on heat transfer characteristics of flow in a channel with fins attached to one wall, 4th International Symposium on Heat Transfer, Beijing, 7–11 Oct 1996. pp. 156 61.
[9] Bastani A, Fiebig M, Mitra NK. Numerical studies of a compact fin-tube heat exchanger, Proceedings of the EUROTHERM Semninar No. 18, Design and Operation of Heat Exchangers, Hamburg, Germany, 27 Feb.–1 Mar. 1991. pp. 154–63.
[10] Jang JY, Wu MC, Chang WJ. Numerical and experimental studies of three-dimensional plate-fin and tube heat exchangers. Int J Heat and Mass Transfer 1996;39(14):3057–66.
[11] Jang JY, Chen LK. Numerical analysis of heat transfer and fluid flow in a three-dimensional wavy-fin and tube heat exchanger. Int J Heat and Mass Transfer 1997;40:3981–90.
[12] Fiebig M, Grosse-Gorgemann A, Chen Y, Mitra NK. Conjugate heat transfer of a finned tube part A : Heat transfer behavior and occurrence of heat transfer reversal. Numerical Heat Transfer, Part A 1995;28:133–46.
[13] ASHRAE Standard 41.1-1986. Standard Method for Temperature Measurement, American Society of Heating, Refrigerating and Air-Conditioning Engineers, Inc., Atlanta, 1986.
[14] ASHRAE Standard 41.2-1987. Standard Method for Laboratory Air-Flow Measurement, American Society of Heating, Refrigerating and Air-Conditioning Engineers, Inc, Atlanta, 1987.
[15] Kay KM, London AL. Compact Heat Exchangers, 3rd edn, McGraw-Hill, New York, 1984.
[16] Moffat RJ. Describing the uncertainties in experimental results. Exp Thermal Fluid Sci 1988;1:3–17.
[17] Van Doormal JP, Raithby GD. Enhancements of the SIMPLE method for predicting incompressible fluid flows. Numerical Heat Transfer 1984;7:147–63.
[18] Schmidt TE. Heat transfer calculations for extended surfaces. Refrigeration engineering 1949;351–7.